Frontiers of Information Technology & Electronic Engineering
www.jzus.zju.edu.cn; engineering.cae.cn; www.springerlink.com
ISSN 2095-9184 (print); ISSN 2095-9230 (online)
E-mail: jzus@zju.edu.cn

Power system design for constant current subsea observatories*

Yan-hu CHEN, Sa XIAO, De-jun LI‡

State Key Laboratory of Fluid Power and Mechatronic Systems, Zhejiang University, Hangzhou 310027, China

E-mail: yanhuchen@zju.edu.cn; sxiao@zju.edu.cn; li_dejun@zju.edu.cn

Received June 7, 2018; Revision accepted Nov. 17, 2018; Crosschecked Nov. 12, 2019

Abstract: Constant current power transmission is considered a good choice for subsea observatories due to its high resistance to shunt faults. A constant current subsea observatory is planned to be constructed in the East China Sea. We discuss a constant current subsea observatory system used for scientific experiments. The power system and its heat dissipation system are carefully designed. The power conversion method is challenging due to the use of constant current power, which is considerably different from traditional power systems. Thus, we adopt power compensation circuits in the conversion system to obtain a constant 48-V output for science users. A power management system that performs overvoltage protection and real-time monitoring and control of junction box is discussed. An innovative heat dissipation structure of a junction box is designed in consideration of a sealed working environment to extend the useful life of the junction box. Simulations and experiments reveal that the system has high efficiency and stability, especially in long-term applications.

Key words: Observatory; Electric energy conversion; Heat dissipation
https://doi.org/10.1631/FITEE.1800362 **CLC number:** TP202

1 Introduction

Humankind has achieved remarkable progress in ocean exploration with the improvement of observatory technology. The study of subsea environment requires scientific instruments, and the power system for an underwater cable network can provide continuous electrical power for science users. Several subsea observatories, such as the cabled observatory system ZERO by Zhejiang University in China (Chen et al., 2012; Wang et al., 2015), the Martha's Vineyard Coastal Observatory, and the Long-term Ecosystem Observatory in the United States (Forrester et al., 1997; Austin et al., 2000; Creed et al., 2005), have been built worldwide.

Traditional terrestrial power systems generally have AC-networked parallel configurations. However, AC transmission through long-distance cables results in high reactive power, which decreases active power for subsea instruments. Thus, AC transmission is used mainly for small-scale observation networks. Constant current (CC) systems have disadvantages such as low power efficiency and expansion difficulty, but CC transmission is superior to DC constant voltage (CV) transmission in resistance to shunt faults. When a shunt fault occurs, the system before the fault can continue to operate with the sea ground location changing instantaneously, whereas a CV system will collapse because it is not resistant to shunt faults. Therefore, the CC method is a better choice than CV in scenarios, where reliability is more important than other features such as efficiency or power delivery capacity (Chen, 2012).

CC observation networks have been established worldwide. Harris and Duennebier (2002) found that the Hawaii Undersea Geo-Observatory (HUGO) delivered approximately 5-kW usable power at the junction box (JBX), which was regulated to 350 V by

‡ Corresponding author

* Project supported by the National Natural Science Foundation of China (No. 41676089), the Natural Science Foundation of Zhejiang Province, China (No. LY18E090003), and the Fundamental Research Funds for the Central Universities, China (No. 2018QNA4005)

ORCID: Yan-hu CHEN , http://orcid.org/0000-0002-5020-7355; De-jun LI, http://orcid.org/0000-0002-9034-4493

a shunt regulator at the JBX, dumping excess power into a resistor stack. The Hawaii-2 Observatory (H2O) (Petitt et al., 2002) delivered a modest 400-W power, with inputs in series and outputs in parallel converters and a shunt regulator in the JBX, which was similar to that of HUGO. The Aloha Cabled Observatory (Howe et al., 2011) in North America used eight converters, 100-V input, and a regulated 48-V output; each converter can provide 160 W, and the power consumed by shunts is controlled by sensing the input voltage to the converter. The versatile eco-monitoring network by under-cable system (Kasahara et al., 2006) delivered 175-W power for science instruments. The dense ocean floor network system for earthquakes and tsunamis (Kawaguchi et al., 2008) in Japan is the backbone cable system and allows loading of up to 3 kW (3 kVDC/1 A). The power distribution control system receives 500-W constant DC power supplied by the terminal equipment and distributes 45-W secondary power output to a measurement instrument circumstances demand. Moreover, the power distribution control system has a mechanism to balance the power consumption of science node constants to prevent the system from reaching an unstable power distribution status. The Marine Cable Hosted Observatory (Hsiao et al., 2014) in Taiwan of China has a total system power supply of 1 kV, 1.1 A.

Based on the abovementioned observatories, some improvements have been made in power conversion topology and heat dissipation systems. Our study is based on these pioneering CC observatories, but we have implemented improvements in the quality and reliability of the systems. We introduce a pulse width modulation (PWM) to drive the power compensation circuit during power conversion rather than using a linear regulator, such as HUGO, H2O, and ACO do, which would shift dissipation power from the semiconductor regulator to the much higher temperature sustainable resistors. We design the two-stage relay control and hardware based on the overvoltage protection circuit to increase the reliability of circuit operation for power management. The power and environmental measurement circuit are added to monitor the power system in real time. We also design an innovative heat dissipation structure for the JBX that dissipates heat directly from the cylinder wall to obtain high dissipating efficiency, thereby increasing reliability for long-term operation. A −1-A CC power supply is used to provide power that serves the entire system and a DC-DC power converter is used to convert the −1-A CC power to a 48-V CV power for science users. The multi-module stacking structure adopted in the power system facilitates the reduction of system volume. Such solutions are important for the future construction of observation networks.

2 System structure

The structure of the CC observation network is illustrated in Fig. 1. The system is responsible for electric energy conversion and data transmission. The electric power from the shore station is transmitted through a long-distance optoelectronic composite cable. In this network, a −1-A CC power is converted into a 48-V CV power for four science instruments. The control system of the JBX conducts data sampling and control. Engineers in the shore station can obtain information from science instruments and realize remote control and real-time monitoring of the observatory.

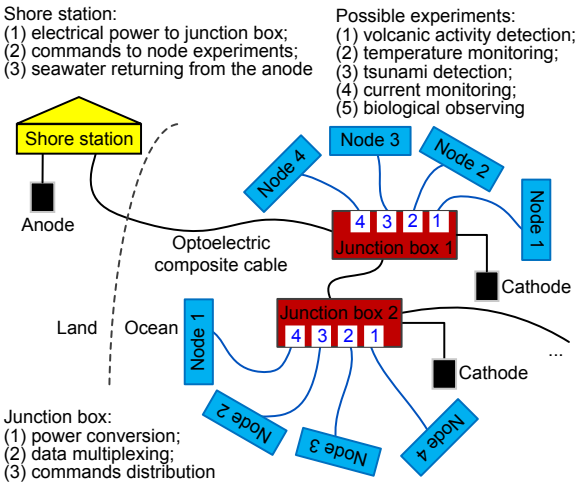

Fig. 1 Structure of a constant current observation network

The power system is constructed with a five-layer architecture, as shown in Fig. 2. The first layer has an overvoltage protection circuit that protects the system in case of overvoltage faults. The second layer has four DC-DC circuits, a 48-V/48-V isolation circuit, a compensation circuit, and a sampling circuit, all of which are responsible for power conversion. The third layer has a power measurement system and

an environmental circuit that provide real-time monitoring of the JBX. The fourth layer includes four relay circuits, which are responsible for performing control actions, such as turning on/off a specific load. The fifth layer has the embedded PC for data processing and control.

3 Power system

3.1 Power conversion

3.1.1 Conversion methods

The power conversion circuit, which includes DC-DC, control, and power compensation circuits, is illustrated in Fig. 3.

To increase the available power, we use multiple converter modules. The turn ratio of the transformer is set to 100:48; thus, if the output voltage is 48 V, the input voltage is −100 V. The output voltage (48 V) floats because there is no direct ground connection for the secondary side. The converters are profoundly different from resistive loads because they present a negative dynamic impedance at the input. This feature means that the input to the converter appears as a constant power load rather than a constant resistance load (Harris and Duennebier, 2002). Considering the −1-A input power, we set the power of a DC-DC circuit to 100 and 400 W for four modules. However, according to Ohm's law, $U=IR$, in which the current I is a constant given by the power supply, the voltage is inconstant when load R_L changes and depends only on an open-loop DC-DC circuit. Thus, the load is set parallel to the power compensation circuit to obtain a constant output voltage. With the sampling circuit, a sampling error amplification signal is converted into a corresponding duty cycle PWM signal that can drive the MOSFET in the power compensation circuit. The power consumed by R_D is controlled by the MOSFET,

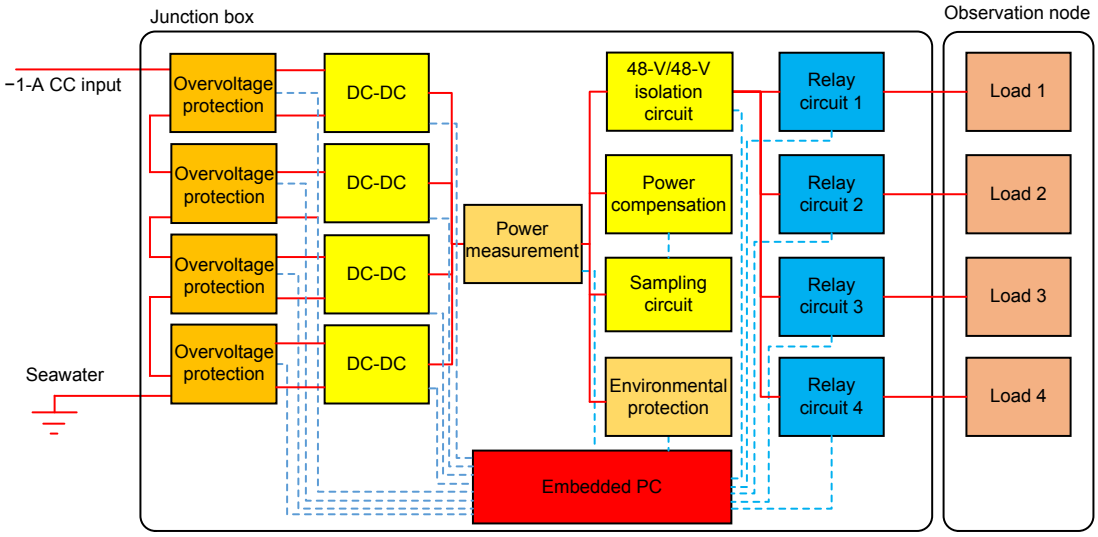

Fig. 2 Design of a power system

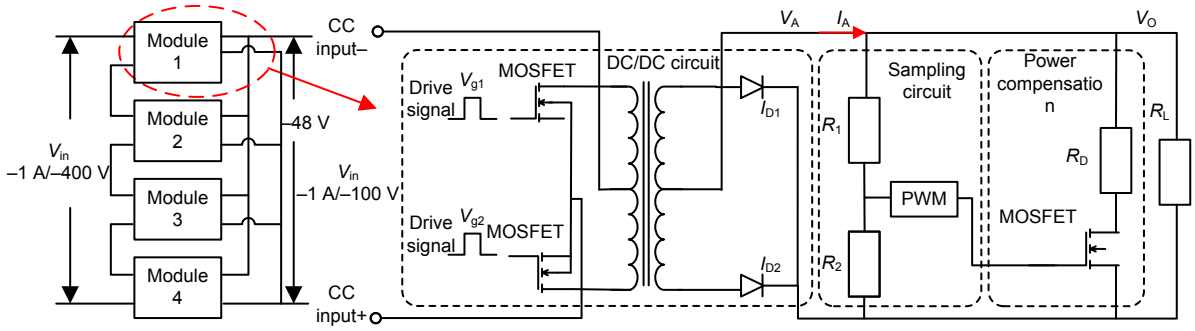

Fig. 3 Designed power conversion circuit

and this compensation power P_{R_D} increases with a decrease in the load power P_{load}. Thus, the total output power P_{total}, which is the sum of P_{load} and P_{R_D}, is constantly 400 W. A constant output voltage is obtained by adopting the power compensation circuit.

3.1.2 Sampling control

The sampling control circuit in Fig. 4 is used for generating a PWM signal for the power compensation circuit. The sampling circuit samples the output voltage and compares this sampling signal with a reference voltage to obtain an error voltage V_e. Proportional-integral-differential (PID) is used to process the error voltage. Then the error voltage is transmitted to an SG3525A driver IC, and the PWM signal is generated by comparing V_p with a saw-toothed wave generated in the chip. The PWM output signal D drives the MOSFET in the power compensation circuit to adjust the output voltage and power.

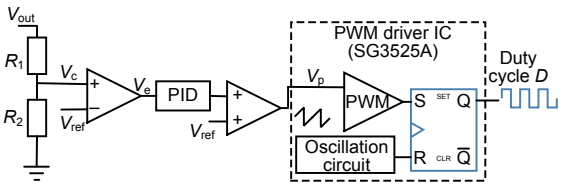

Fig. 4 Structure of the sampling circuit

V_{out} is the output voltage of the power conversion circuit, V_c is the sampling voltage, and K_c is the sampling rate which equals R_2/R_1. The relationship between V_c and V_{out} can be written as

$$V_c = V_{out} K_c. \tag{1}$$

For the PID control, a proportional component K_p is adopted to obtain a favorable control performance. Thus, the input voltage V_p of the PWM driver IC can be written as

$$V_p = (V_c - V_{ref}) K_p + V_{ref}. \tag{2}$$

By substituting Eq. (1) into Eq. (2), we obtain

$$V_{out} = \frac{V_p + (K_p - 1)V_{ref}}{K_c K_p}. \tag{3}$$

If V_p<0.9 V, the power compensation circuit will not function when the system starts. If V_p=V_{pl}=0.9 V (i.e., V_{out}=V_l), then the power compensation circuit functions. When V_{out} reaches the maximum adjustable value V_h (V_p=V_{ph}=3.3 V), the power compensation circuit works when V_{pl}<V_p<V_{ph} (i.e., V_l<V_{out}<V_h). By substituting K_c=3.3/48 and V_{ref}=3.3 V into Eq. (3), we obtain

$$V_l = \frac{V_{pl} + (K_p - 1)V_{ref}}{K_c K_p} = 48 - \frac{384}{11K_p}, \tag{4}$$

$$V_h = \frac{V_{ph} + (K_p - 1)V_{ref}}{K_c K_p} = 48. \tag{5}$$

From Eqs. (4) and (5), the output voltage ripple ΔV under the effect of the power compensation circuit can be written as

$$\Delta V = V_h - V_l = \frac{384}{11K_p}. \tag{6}$$

Eq. (6) indicates that an inverse proportional relationship exists between ΔV and K_p, and that K_p>69.82 can make ΔV lower than 0.5 V, which satisfies the requirements.

3.1.3 Simulation results

To evaluate the performance of the proposed methods, we established a simulation model of the power conversion circuit shown in Fig. 3 in Pspice. Two different scenarios were simulated by turning on the load at 0.1 s and turning off at 0.2 s. The resultant path is illustrated in Fig. 5.

The overshoot of voltage at the beginning returns to normal levels due to the influence of the

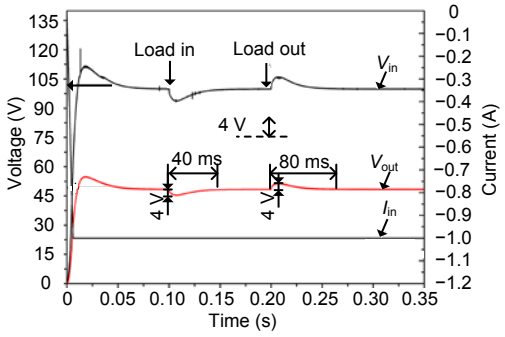

Fig. 5 Simulation waveform of the power conversion circuit

compensation circuit. When the load is turned on at 0.1 s, a large starting current causes a 4-V output voltage to drop. Then, approximately 0.04 s later, the voltage returns to 48 V due to the effect of the power compensation circuit. When the load is turned off at 0.2 s, the decreased load power causes an output voltage rise, and the output voltage returns to 48 V after approximately 0.08 s. Simulation results confirm that the converter works well under various load conditions.

3.2 Power management

Power management circuits can provide protection, control, or measurement to the system. In this subsection, we discuss mainly the overvoltage protection, power and environmental measurement, and relay control circuits.

3.2.1 Overvoltage protection

An overvoltage protection circuit is required to protect the system in case of overvoltage faults. An improved crowbar circuit (Fig. 6) can provide automatic overvoltage protection, active bypass protection, and a reset function to the system. The silicon-controlled rectifier (SCR) is turned on when the input voltage exceeds the Zener reverse bias voltage *Dz*, resulting in the isolation of the main circuit. This SCR action is called automatic overvoltage protection. An active control is added to the crowbar circuit to improve its controllability. An external bypass signal activates the optocoupler, which consequently turns on the SCR to realize the active bypass function. A reset circuit must be used to turn off the SCR because the SCR is uncontrollable by its control after it is activated. The reset circuit is similar to the bypass circuit; an external reset signal turns on the MOSFET, thereby decreasing the current that flows through the SCR, and the SCR is turned off as a result.

3.2.2 Power and environmental measurement

The power measurement circuit is used to timely monitor the voltage and current. The circuit structure is illustrated in Fig. 7. The electric sampling module used for voltage or current detection can work in temperatures ranging from –25 °C to 71 °C and has a linearity of 0.1%, a sampling accuracy of 0.1%, and a maximum temperature drift of 50 PPM/°C. A current detection circuit is placed before the power compensation and load isolation circuits obtain the power of each circuit. A 48-V to 24-V voltage conversion circuit is installed for the environmental monitoring circuit.

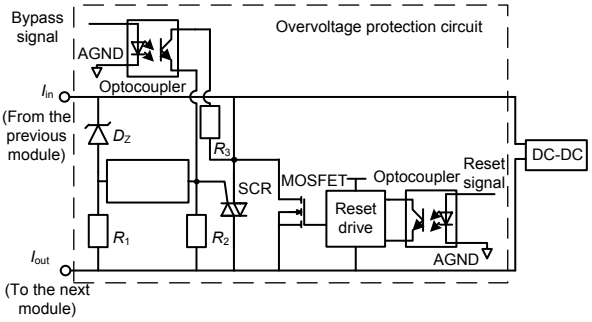

Fig. 6 Improved crowbar circuit

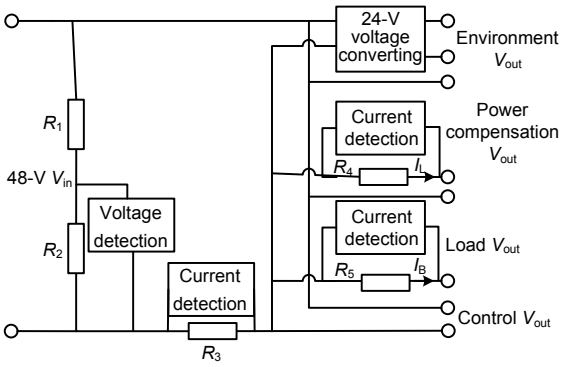

Fig. 7 Structure of the power measurement circuit

Circuits are encapsulated in a pressure case in the deep sea. Therefore, measuring the environment inside the case is indispensable in cases of unexpected faults. Environmental measurement includes mainly temperature, humidity, and water leakage. The resolving power of the temperature sensor is 0.01 V/°C, and the temperature measurement accuracy is 0.5 °C. Moreover, the resolving power of the humidity sensor is 0.03 V/(% RH), and the accuracy is ±3%. When water leakage occurs, the humidity in the pressure case will not rise immediately. Thus, a sensor is needed to ensure water leakage detection in real time. The water leakage lines are two conductors placed at the bottom of the pressure case. Hence, if water leakage occurs, the leakage sensor will work. The resistance between the two lines, which is at the GΩ level in normal condition, will vary from a few to tens of ohms depending on how much the conductor is exposed to seawater. Therefore, the water leakage

condition inside the case can be obtained by measuring the resistance between two conductors.

3.2.3 Relay control

Semiconductors, such as MOSFET, can quickly interrupt large currents with a relatively small size. So, we use MOSFETs to interrupt work current first, and then use a mechanical relay to cut the leakage current to realize physical isolation from seawater. In this manner, the mechanical relay will not be subjected to any considerable current that can potentially cause contact failures. The relay circuit in Fig. 8 is used mainly to reliably turn specific loads on/off and to conduct failure isolation. When turning on the load, the mechanical relay is turned on first, followed by the MOSFETs. When turning off the load, the MOSFETs are turned off first, followed by the mechanical relay. The circuit can attain electrical isolation and achieve fast response through the two-stage relay control, which combines mechanical relay and MOSFETs. Simultaneously, the circuit avoids the electric arc generated by the relay operations and prolongs the system life span. In addition, the parallel use of dual MOSFETs increases the reliability of the circuit operation.

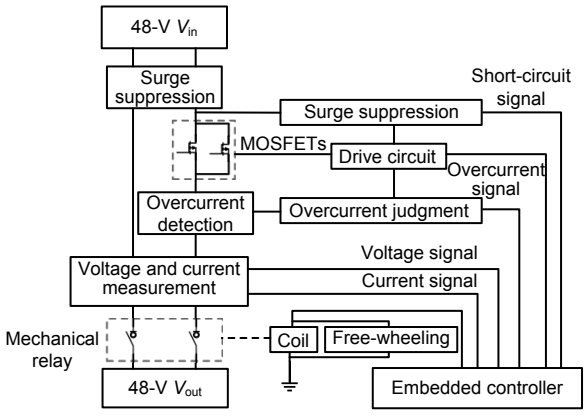

Fig. 8 Relay control circuit

4 Theoretical analysis of heat dissipation

The appropriate heat management of an electronic apparatus exerts considerable influence on the useful life of JBXs (Toma et al., 2015). In this section, we investigate a proper and innovative heat dissipation strategy for JBXs. Fig. 9 displays the thermal structure of the case. The material used for the radiating plate is aluminum, and the case is made of titanium alloy. Thermal grease is smeared on the contact gap between the power resistor and radiating plate and between the pressure case and radiating plate. The heat source (power resistor) is at constant power, and the system is at constant temperature in a steady state.

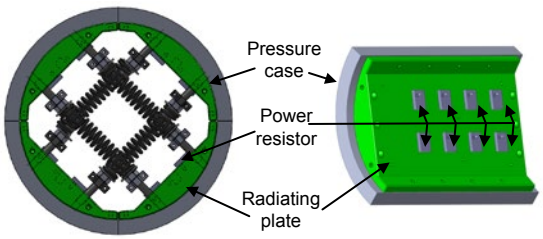

Fig. 9 Structure of the case

Assume that the case is a cylinder. Fig. 10 shows the cylindrical coordinate system.

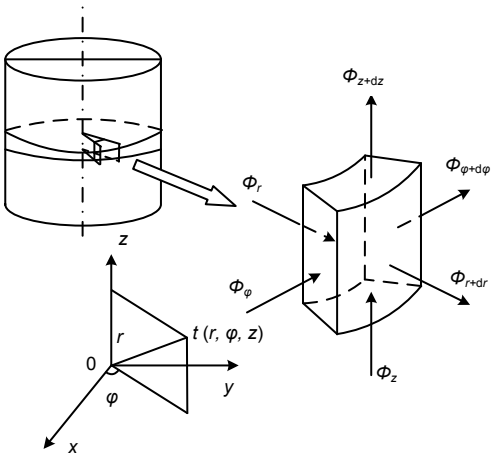

Fig. 10 Cylindrical coordinate system

The infinitesimal method is used to analyze the heat dissipation of the system. The heat conduction differential equation of the infinitesimal hexahedron can be written as

$$\rho c\frac{\partial t}{\partial \tau}=\frac{1}{r}\frac{\partial}{\partial r}\left(\lambda r\frac{\partial t}{\partial r}\right)+\frac{1}{r^2}\frac{\partial}{\partial \varphi}\left(\lambda\frac{\partial t}{\partial \varphi}\right)+\frac{\partial}{\partial z}\left(\lambda\frac{\partial t}{\partial z}\right)+\Phi_{\mathrm{v}}, \tag{7}$$

where ρ denotes case density, c the specific heat, and Φ_{v} the heat of formation in unit time and volume.

The temperature of the case is constant when in a steady state (i.e., $\rho c\partial t/\partial\tau$=0) and the temperature of an exact hexahedron is independent of φ and z; thus,

$\partial t/\partial\varphi=\partial t/\partial z=0$. The simplified heat conduction differential equation can be written as follows:

$$\frac{\mathrm{d}}{\mathrm{d}r}\left(r\frac{\mathrm{d}t}{\mathrm{d}r}\right)=0. \tag{8}$$

For clarity, the cross section of the pressure case is depicted in Fig. 11.

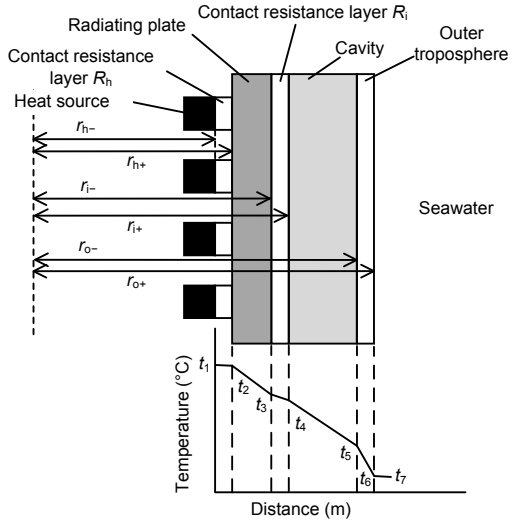

Fig. 11 Cross section of the case

The heat transfer formula of every layer can be calculated by integrating Eq. (8), expressed as

$$\begin{cases} t_1-t_2=R_\mathrm{h}\Phi, & r_{\mathrm{h}-}<r\le r_{\mathrm{h}+},\\ t=a_1\ln r+a_2, & r_{\mathrm{h}+}<r\le r_{\mathrm{i}-},\\ t_3-t_4=R_\mathrm{i}\Phi, & r_{\mathrm{i}-}<r\le r_{\mathrm{i}+},\\ t=a_3\ln r+a_4, & r_{\mathrm{i}+}<r\le r_{\mathrm{o}-},\\ t_5-t_6=\Phi/(hA), & r_{\mathrm{o}-}<r\le r_{\mathrm{o}+}, \end{cases} \tag{9}$$

with the boundary conditions expressed as

$$\Phi=\begin{cases} -\lambda_1\cdot 2\pi r_{\mathrm{h}+}l\left.\dfrac{\mathrm{d}t}{\mathrm{d}r}\right|_{r=r_{\mathrm{h}+}},\\ -\lambda_1\cdot 2\pi r_{\mathrm{i}-}l\left.\dfrac{\mathrm{d}t}{\mathrm{d}r}\right|_{r=r_{\mathrm{i}-}},\\ -\lambda_2\cdot 2\pi r_{\mathrm{i}+}l\left.\dfrac{\mathrm{d}t}{\mathrm{d}r}\right|_{r=r_{\mathrm{i}+}},\\ -\lambda_2\cdot 2\pi r_{\mathrm{o}-}l\left.\dfrac{\mathrm{d}t}{\mathrm{d}r}\right|_{r=r_{\mathrm{o}-}}, \end{cases} \tag{10}$$

where λ_1 and λ_2 are the thermal conductivities of the radiating plate and case wall respectively, l the length of the radiating plate, h the convective heat transfer coefficient between the case and seawater, R the contact thermal resistance of the contact resistance layer, A the heat transfer area, Φ the volume heat, and a_1–a_4 the integral constants.

Then, a_1–a_4 can be calculated by Eqs. (9) and (10), expressed as

$$\begin{cases} a_1=\dfrac{\Phi}{-\lambda_1\cdot 2\pi l},\\ a_2=R_\mathrm{l}\Phi+\dfrac{\Phi\ln(r_{\mathrm{o}-}/r_{\mathrm{i}+})}{\lambda_2\cdot 2\pi l}+\dfrac{\Phi\ln r_{\mathrm{i}-}}{\lambda_1\cdot 2\pi l}+\dfrac{\Phi}{hA}+t_6,\\ a_3=\dfrac{\Phi}{-\lambda_2\cdot 2\pi l},\\ a_4=\dfrac{\Phi\ln r_{\mathrm{o}-}}{\lambda_2\cdot 2\pi l}+\dfrac{\Phi}{hA}+t_6. \end{cases} \tag{11}$$

Thermal grease is dispensed between the heat source and radiating plate. Thus, the contact thermal resistance R_h can be considered as zero. t_6 is equal to seawater temperature t_7, where t_7=2 °C.

The contact resistance R_i between the radiating plate and case can be calculated (Yovanovich, 2000, 2005; Bahrami et al., 2004; Gong and Yang, 2007; Luo et al., 2011; Lv et al., 2014); $R_\mathrm{i}=4.3\times10^{-2}$ K/W.

The current velocity of deep seawater is approximately zero. Therefore, the correlation in large-space natural convection experiments can be considered as follows:

$$N_{\mu_p}=C(G_\mathrm{r}P_\mathrm{r})_p^q, \tag{12}$$

where N_{μ_p} is the N_μ, which is composed of the average surface heat transfer coefficient, C and q are parameters of the experiments, p denotes the arithmetic mean temperature of the boundary layer ($t_p=(t_5+t_7)/2$), G_r is a Grashof number, and P_r is a Prandtl number.

$$G_\mathrm{r}=ga_\mathrm{v}V_\mathrm{t}l^3/\nu^2, \tag{13}$$

$$P_\mathrm{r}=\mu c_\mathrm{p}/\lambda=\nu/\alpha, \tag{14}$$

where g is the acceleration of gravity, a_v the

coefficient of volume change, V_t the temperature difference between the case surface and seawater, v the kinematic viscosity, and α the thermal diffusivity.

The convective heat transfer coefficient h is obtained through the definition of N_μ:

$$N_\mu = \frac{hl}{\lambda_3}, \tag{15}$$

where λ_3 is the thermal conductivity of seawater. Different from Eq. (9), h is recalculated until an appropriate h is obtained. Subsequently, we derive h=326 W/(m^2×K). a_1–a_4 are obtained by substituting R_i and h into Eq. (11). Finally, the mathematical model of the system is constructed.

A case model is established in ANSYS by the given R_i, R_h, and h for a simulated validation of the simplified temperature field in Eq. (9). The simulation is conducted at two different power levels: 100 and 350 W. The maximum temperatures, which appear on the heat dissipation surface of the power resistor, are approximately 25.4 °C and 34.6 °C (Fig. 12). From Eq. (9), we can obtain t_1=37 °C when the power compensation circuit is working under 350 W and t_1=22 °C when the power compensation circuit is working under 100 W. The simulated and theoretical results do not differ significantly. Therefore, the theoretical model is suitable for practical engineering applications.

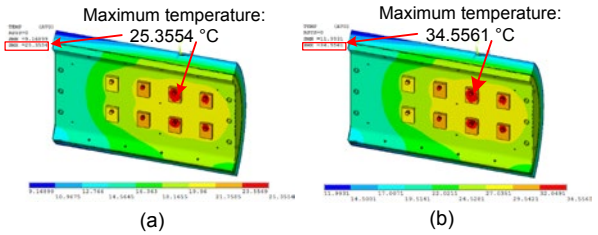

Fig. 12 Temperature distribution under 100 W (a) and 350 W (b)

5 Laboratory tests of the prototype

5.1 Test of the power conversion methods

The power conversion methods designed in Section 3.1 indicate a favorable performance according to the simulation. In this subsection, a test was conducted to verify these methods. As shown in Fig. 13a, the compensation circuit began working a few minutes after the system started, and the output voltage remained stable at 48 V approximately 150 ms later. In Fig. 13b, a drop of approximately 8 V occurred for the output side when a 32-Ω load was connected in the circuit, and the output remained at 48 V approximately 40 ms later. In Fig. 13c, an increase of approximately 5 V occurred for the output side when the 32-Ω load was disconnected, and the output remained at 48 V approximately 80 ms later. Experimental results were consistent with the simulation results in Fig. 5, indicating that the power conversion methods were reliable and stable for actual operations.

5.2 Tests of the overvoltage protection function

Several tests were performed to verify the overvoltage protection function. The input current was slowly increased until the input voltage exceeded the Zener reverse bias voltage; then, the overvoltage protection circuit started working. The SCR was turned on to shorten the output branch. The oscilloscope images of the voltage for the input and output sides are presented in Fig. 14a, which shows that the overvoltage process was completed in 8 ms when the input voltage was increased to approximately 131.2 V. The output voltage protection process ended in 40 ms because of the time needed to charge the capacitor. The active bypass and reset functions were verified after the automatic overvoltage protection function was verified. An external bypass signal was provided to the circuit under normal working conditions to bypass the output branch. The voltage fluctuation is displayed in Fig. 14b. The voltage decreased to zero after receiving the bypass signal, thereby indicating that the active bypass protection function was activated. Reset signal was transmitted to the overvoltage protection circuit. The corresponding voltages are illustrated in Fig. 14c, which depicts a voltage overshoot of 70 V for the output side during the initial 0.25 s. Then the output voltage remained at 48 V at 0.3 s after sending the reset signal to the circuit. These three tests verified the reliability of the overvoltage protection function, which satisfied the requirements.

5.3 Tests of the heat dissipation

The test on the heat dissipation system could indicate whether a closed case is reasonable. The system was working in a rated state and had no load. Thus, the input power was consumed by the power

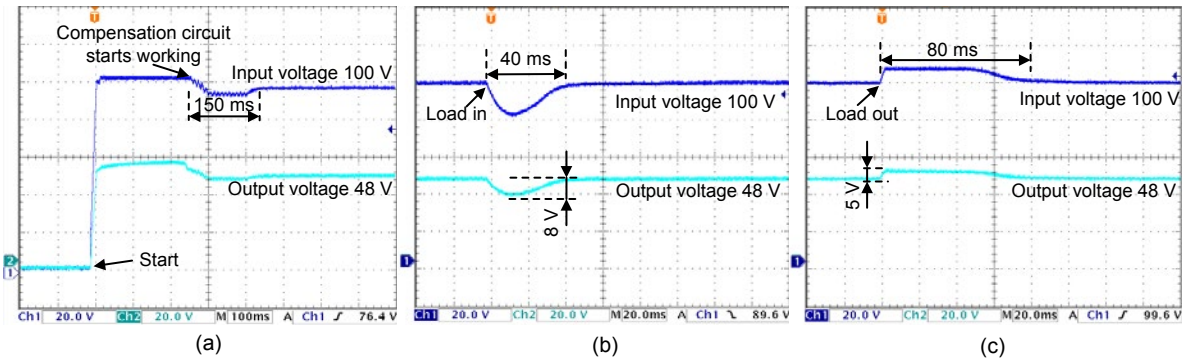

Fig. 13 Waveforms of the power conversion methods: (a) startup characteristics; (b) load in; (c) load out

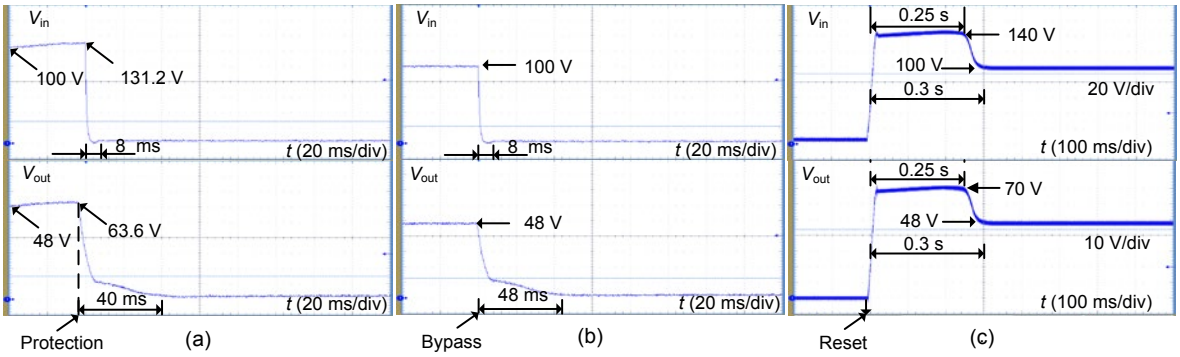

Fig. 14 Waveforms of the overvoltage protection function: (a) automatic overvoltage protection; (b) bypass operation; (c) reset operation

compensation circuit. In this case, the system generated the maximum amount of heat. The temperature distribution is depicted in Fig. 15. The highest temperature appeared on the surface of the transformer and power resistor when the system was in a steady state. The room temperature was 18 °C during the test, and the temperature of the transformer increased to 19 °C, which was lower than the allowable temperature rise (25 °C). The temperature rise of the power resistor was approximately 30 °C, which was far below the ultimate temperature of these resistors.

The actual working environment is different from a lab environment, because the case is under water. By contrast, heat dissipation is easily facilitated underwater. Therefore, the temperature rise in working conditions cannot reach the temperature level in a lab test. Thus, this prototype satisfies requirements.

Another temperature rise test was performed. In this test, the case was placed underwater, and the system was working in a rated state and had no load. We obtained the temperatures from four sensors

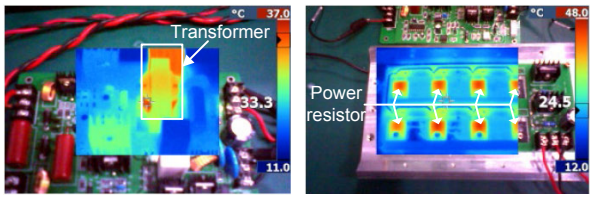

Fig. 15 Temperature of the transformer (a) and power resistor (b)

distributed inside the case (surface of the radiating plate, air near the radiating plate, air near the CC/CV module, and air around the embedded controller) after the system had been working continuously over 24 h. The highest temperature was approximately 29 °C just on the surface of the radiating plate. The test results indicate that the temperature rise was low enough that the effect on long-term reliability could be minimal.

5.4 Test of the prototype

Design specifications indicate that the case must satisfy strength requirements and resist high water

pressure to ensure that no water leakage occurs. Assuming that the working depth of the case is 2000 m and that the test pressure is 1.25 times greater than the design pressure (20 MPa) according to the marine instrumentation standards, the test pressure was set to 26 MPa to simulate water pressure. Results showed that the case pressure strength satisfied the requirements.

The laboratory test on the prototype is shown in Fig. 16. The system was set to operate continuously 4 h after the strength test verified its working reliability. The topology and results of the test are depicted in Fig. 17.

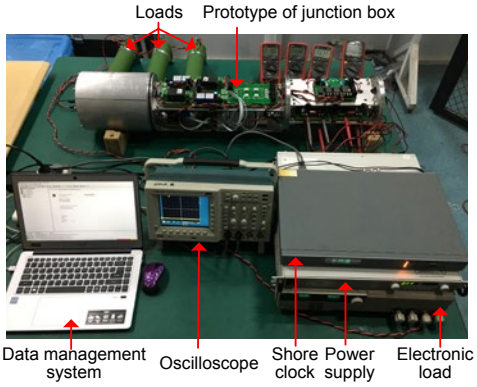

Fig. 16 Laboratory tests on the prototype

Fig. 17 demonstrates that the voltage or current was constant during normal operations. The load voltage stabilized at 48 V, and the output voltage ripple ΔV, which was approximately 0.5 V, fitted our design of the sampling control circuit. The temperature was approximately 20 °C, which was within the limits of the heat dissipation requirements. Finally, a water pool test of the prototype was performed to verify the underwater performance of the JBX. Results verified the stability and reliability of the prototype.

6 Conclusions

A subsea observatory system has been investigated for delivering continuous power to subsea instruments. In this study, we have presented all the sections of the system, i.e., power conversion, power management, and heat dissipation analysis. The proposed method is different from typical power delivery approaches because it uses a direct CC. Therefore, a new conversion topology for a −1-A CC power to a 48-V CV power conversion has been proposed. The loads have been set parallel to the

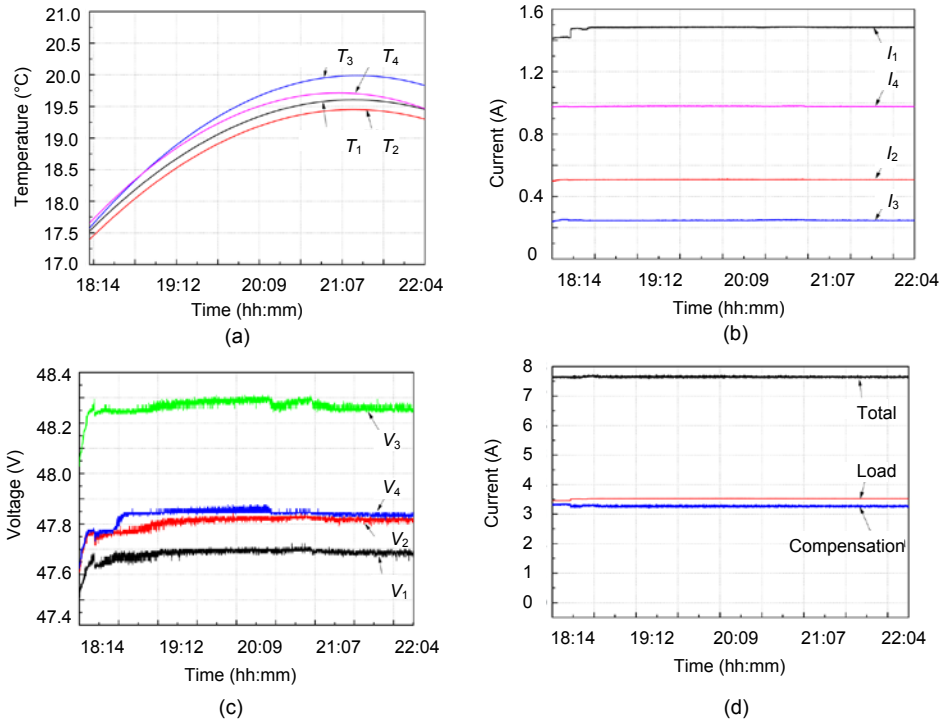

Fig. 17 Results of the laboratory tests: (a) temperature of four DC-DC circuits; (b) output currents of four DC-DC circuits; (c) output voltages of four DC-DC circuits; (d) currents of power measurement

PWM-controlled power compensation circuit to obtain a constant output voltage. The power management system, including overvoltage protection, power and environmental measurement, and relay control, has been thoroughly discussed. The heat dissipation in the case has been analyzed in detail. Experimental results showed that these designs meet the requirements. The CC subsea observatory is valuable for subsea research. Future work will focus on improving the stability and reliability of the multi-node system.

Compliance with ethics guidelines

Yan-hu CHEN, Sa XIAO, and De-jun LI declare that they have no conflict of interest.

References

Austin T, Edson J, McGillis W, et al., 2000. The Martha's Vineyard Coastal Observatory: a long term facility for monitoring air-sea processes. Proc OCEANS MTS/IEEE Conf and Exhibition, p.1937-1941. https://doi.org/10.1109/OCEANS.2000.882223

Bahrami M, Yovanovich MM, Culham JR, 2004. Thermal joint resistances of conforming rough surfaces with gas-filled gaps. *J Thermophys Heat Trans*, 18(3):318-325. https://doi.org/10.2514/1.5480

Chen YH, 2012. Research on the Key Technologies of Power Junction for Cabled Ocean Observatories System based on Tree Topology. PhD Thesis, Zhejiang University, China (in Chinese).

Chen YH, Yang CJ, Li DJ, et al., 2012. Development of a direct current power system for a multi-node cabled ocean observatory system. *J Zhejiang Univ-Sci C* (*Comput & Electron*), 13(8):613-623. https://doi.org/10.1631/jzus.C1100381

Creed EL, Glenn S, Schofield OM, et al., 2005. LEO-15 Observatory—the next generation. Proc OCEANS MTS/IEEE Conf and Exhibition, p.657-661. https://doi.org/10.1109/OCEANS.2005.1639828

Forrester NC, Stokey RP, von Alt C, et al., 1997. The LEO-15 Long-term Ecosystem Observatory: design and installation. Proc MTS/IEEE Conf and Exhibition, p.1082-1088. https://doi.org/10.1109/OCEANS.1997.624142

Gong Z, Yang CX, 2007. The simplification of the thermal contact conductance model. *J Eng Thermophys*, 28(5): 850-852.

Harris DW, Duennebier FK, 2002. Powering cabled ocean-bottom observatories. *IEEE J Ocean Eng*, 27(2):202-211. https://doi.org/10.1109/JOE.2002.1002474

Howe BM, Lukas R, Duennebier F, et al., 2011. ALOHA Cabled Observatory installation. Proc OCEANS MTS/IEEE KONA, p.1-11. https://doi.org/10.23919/OCEANS.2011.6107301

Hsiao NC, Lin TW, Hsu SK, et al., 2014. Improvement of earthquake locations with the Marine Cable Hosted Observatory (MACHO) offshore NE Taiwan. *Mar Geophys Res*, 35(3):327-336. https://doi.org/10.1007/s11001-013-9207-3

Kasahara J, Iwase R, Nakatsuka T, et al., 2006. An Experimental Multi-Disciplinary Observatory (VENUS) at the Ryukyu Trench using the Guam-Okinawa Geophysical Submarine Cable. *Ann Geophys*, 49(2-3):595-606.

Kawaguchi K, Kaneda Y, Araki E, 2008. The DONET: a real-time seafloor research infrastructure for the precise earthquake and tsunami monitoring. Proc OCEANS MTS/IEEE Kobe Techno-Ocean, p.1-4. https://doi.org/10.1109/OCEANSKOBE.2008.4530918

Luo XB, Feng H, Liu J, et al., 2011. An experimental investigation on thermal contact resistance across metal contact interfaces. Proc 12th Int Conf on Electronic Packaging Technology and High Density Packaging, p.1-6. https://doi.org/10.1109/ICEPT.2011.6066936

Lv GY, Dong YG, Zhang CN, et al., 2014. Numerical simulation and analysis of contact thermal resistance on motor controller based on Matlab. Proc IEEE Conf and Expo Transportation Electrification Asia-Pacific, p.1-4. https://doi.org/10.1109/ITEC-AP.2014.6940623

Petitt RA, Harris DW, Wooding B, et al., 2002. The Hawaii-2 Observatory. *IEEE J Ocean Eng*, 27(2):245-253. https://doi.org/10.1109/JOE.2002.1002479

Toma DM, Mànuel-Làzaro A, Nogueras M, et al., 2015. Study on heat dissipation and cooling optimization of the junction box of OBSEA seafloor observatory. *IEEE/ASME Trans Mechatron*, 20(3):1301-1309. https://doi.org/10.1109/TMECH.2014.2336791

Wang J, Li DJ, Yang CJ, et al., 2015. Developing a power monitoring and protection system for the junction boxes of an experimental seafloor observatory network. *Front Inform Technol Electron Eng*, 16(12):1034-1045. https://doi.org/10.1631/FITEE.1500099

Yovanovich MM, 2000. Thermal-mechanical models for non-conforming surface contacts. Proc 7th Intersociety Conf on Thermal and Thermomechanical Phenomena in Electronic Systems, p.290-295. https://doi.org/10.1109/ITHERM.2000.866838

Yovanovich MM, 2005. Four decades of research on thermal contact, gap, and joint resistance in microelectronics. *IEEE Trans Compon Pack Technol*, 28(2):182-206. https://doi.org/10.1109/TCAPT.2005.848483